

Automated Recognition of Post-Flare Loops in High-Resolution $H\alpha$ Red-Wing Images

Meng Yang^{1,2,3,4,5} • Xiaoying Gong^{1,2,3,6} • Yangyi Liu^{1,2,7,8} • Yu Tian^{1,2} • Changhui Rao^{1,2,3}

Received: 29 June 2018 / Accepted: 28 April 2022 / Published online: 25 May 2022 © The Author(s), under exclusive licence to Springer Nature B.V. 2022

Abstract

The post-flare loop is a typical dynamic process of solar flares. In the past, a manual method was used to recognize the strand structure of loops. With higher spatial resolving power, the post-flare loop consists of more bundles of strands. For fast and reliable post-flare-loop recognition, an automated post-flare-loop detection method applied to high-resolution H α red-wing images is proposed in this article. In this method, straight lines are detected from the edge-detection result, and then a curve-growing procedure is carried out on the basis of the detected straight lines. Finally, the grown curves are screened to eliminate isolated and intersected curves. To our knowledge, our research is the first trial to detect post-flare loops on the solar disk. Experimental results with the high-resolution H α red-wing images from the *Goode Solar Telescope* (GST) have verified that the proposed method could detect post-flare loops effectively in all their developing phases. Based on the recognition results, the automatically computed loop widths (118 \pm 35 km) are consistent with the manually derived results (124 \pm 19 km). With the development of observing instrumentation, the proposed method may recognize each strand of the loops and the measured loop widths could be used to verify flare models.

Keywords Flares · Models · Instrumentation and data management

C. Rao chrao@ioe.ac.cn

- Key Laboratory on Adaptive Optics, Chinese Academy of Sciences, Chengdu, Sichuan 610209, China
- Institute of Optics and Electronics, Chinese Academy of Sciences, Chengdu, Sichuan 610209, China
- University of Chinese Academy of Sciences, Beijing 100049, China
- Science and Technology on Electromagnetic Compatibility Laboratory, Wuhan 430064, China
- China Ship Development and Design Center, Wuhan 430064, China
- School of Electronic, Electrical and Communication Engineering, University of Chinese Academy of Sciences, Beijing 100049, China
- ⁷ Sichuan Police College, Luzhou, 646000, China
- 8 Intelligent Policing Key Laboratory of Sichuan Province, Luzhou, 646000, China



62 Page 2 of 14 M. Yang et al.

1. Introduction

Post-flare loops are significant and enduring features accompanying typical large two-ribbon flares, and these loops are overlapped and inlaid on one another in H α images (Lin et al., 1992). The loops are anchored in the chromosphere, which is most likely the source of the dense plasma in the hot loops (Podgorny and Podgorny, 2002). It is generally believed that magnetic reconnection plays an important role in the formation and evolution of the post-flare loops. To be more specific, the rise and expansion of post-flare loops are essentially due to the continuous increase in magnetic flux, which has enhanced the magnetic pressure underneath the post-flare-loop system (Cheng et al., 2010). Post-flare loops are usually observed in the H α , X-ray and EUV bands. They are first observed in soft X-rays when the temperature reaches 10^7 K, then observed in the coronal spectra when the temperature is about 10^6 K, and observed in the H α band when the plasma has cooled down to 10^4 K.

As the wavelength is shifted from Hα line-center towards the red-wing, post-flare loops become more noticeable (Antolin and Rouppe van der Voort, 2012), thus they are often observed in the Hα red-wing images. Most observations of post-flare loops concentrate on the solar limb (Kamio, Kurokawa, and Ishii, 2003; Srivastava et al., 2008; White, Verwichte, and Foullon, 2012). Taking advantage of the resolving power of the *Swedish 1-m Solar Telescope* (SST)/*CRisp Imaging Spectro-Polarimeter* (CRISP: Scharmer et al., 2008) and the 1.6-m *Goode Solar Telescope* (GST)/*Visible Imaging Spectrometer* (VIS: Cao et al., 2010), the fine structures of the post-flare loops can be observed in high resolution on the solar disk.

However, the post-flare loop is not a monolithic structure. Both MHD simulations and hydrodynamic simulations conclude that each loop consists of a bundle of unresolved and tangled strands that were heated at different times (Klimchuk, 2006). Each strand is characterized by a uniform temperature and density (Cargill, 1994). The width or cross-sectional area of each strand is an important parameter in calculating the filling factor and the energy of a nanoflare (Sakamoto, Tsuneta, and Vekstein, 2008). Once the density is determined, the width for each strand can also be used to derive the emission measure (Reeves and Warren, 2002).

The width of each strand specified by Cargill (1994), Cargill and Klimchuk (2004), and Vekstein (2009) is about 100 km, 15 km, and 20 km, respectively. Recently, the cross-sectional width of each strand was measured by labeling the cross-section slits of these loops manually in Hα red-wing images, and it turns out to be about 124 km (Jing et al., 2016). However, it is demonstrated that the actual fine-scale of post-flare loops is much below 100 km and is beyond the observational capabilities of the most powerful ground-based instrumentation available (Scullion et al., 2014). The fine structure of the strands within a single loop may be revealed by future telescopes with larger apertures, e.g. the 4-m aperture *Daniel K. Inouye Solar Telescope* (DKIST: Rimmele et al., 2020). However, the manual method is not able to handle huge amounts of image data and needs to be replaced by an automated method. The automated recognition of post-flare loops is the first step to calculate the strand width, and the recognition result may also be used to explore the topological structure of the local coronal magnetic field and the origin of solar coronal heating (Scullion et al., 2014).

To our knowledge, automated post-flare-loop recognition methods on the solar disk have not been studied in the literature, but investigating the recognition methods of other similar features, e.g. coronal loops, may be helpful. Both coronal loops and post-flare loops follow the magnetic field and thus have elliptical shapes, large curvature radii, and can be traced with oriented-directivity methods (Aschwanden, 2010). Some image-processing



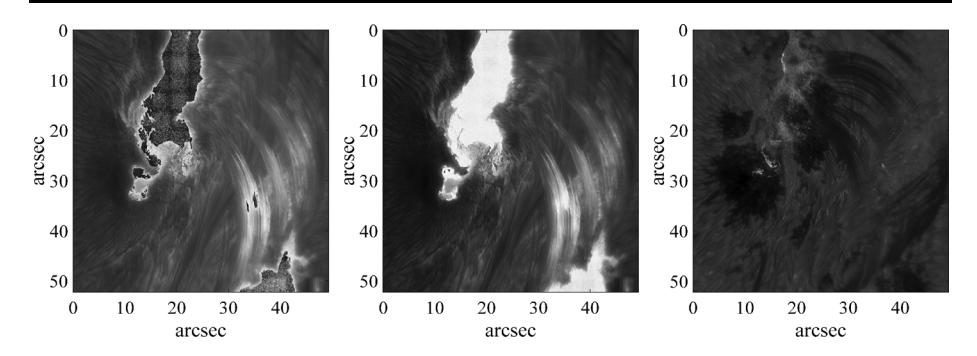


Figure 1 The speckle-reconstructed images in 6563+0.0 Å (*left*) and 6563+1.0 Å (*right*) of a part of NOAA AR 12371 from GST at 18:28 UT on 22 June 2015. The image in the *middle* is the pre-processed image on the left.

and machine-learning techniques are used in coronal-loop detection methods, such as ellipse detection and inverse Hough transform (Sellah and Nasraoui, 2008), ridge detection based on image gradients (Inhester, Feng, and Wiegelmann, 2008), supervised neural network learning (Durak, Nasraoui, and Schmelz, 2009), wavelet-transform (McAteer et al., 2010), a method similar to region-growing (Aschwanden, 2010), and so on.

In this article, a hybrid method that combines edge detection, Hough transform, and curve growing is proposed to recognize post-flare loops in the multiple frames of high-resolution $H\alpha$ red-wing images. Firstly, edges are detected using gradient information. Secondly, straight lines are recognized by a Hough transform of the edges. Then, these straight lines are extended into curves in a curve-growing process, and the flaring region is segmented from the $H\alpha$ line-center image and used to determine the blending orientation. Finally, isolated and intersected curves are eliminated to reduce the false-positive rate of loop detection.

The article is organized as follows: The observations are presented in Section 2. Section 3 describes the post-flare recognition process in detail. In Section 4, experimental results on GST H α red-wing images are given to validate the effectiveness of the proposed method, and the widths along the loops are measured. Section 5 summarizes the proposed method and concludes the article.

2. Data Sources

The high-resolution $H\alpha$ red-wing and line-center observations in this article are provided by the GST/VIS at the Big Bear Solar Observatory (BBSO) (Denker et al., 1999). GST/VIS observations in the $H\alpha$ 6563 Å line-center and off-bands (± 0.6 Å and ± 1.0 Å) can achieve a pixel size as small as 0.03", and its field-of-view is $57'' \times 64''$. The flare observations in this article appeared in NOAA active region (AR) 12371 on 22 June 2015. The GST/VIS $H\alpha$ image sequences are from 17:14 to 19:35 at a 28-second cadence. All time references in this article are in Universal Time (UT). Data from GST/VIS could be requested via the online GST Data Request Form at www.bbso.njit.edu/~vayur/NST_catalog/.

The line-center image, as shown in the left image of Figure 1, is used to segment the flaring region. The post-flare-loop detection is carried out in the red-wing image, as shown in the right image of Figure 1. However, there are some dark points within the flaring region to be removed in the line-center image (Yang et al., 2018). This can be achieved by



implementing

$$\operatorname{Img}'(x) = \begin{cases} \operatorname{Img}(x) &, \max(\operatorname{Img}_{5 \times 5}(x)) - \operatorname{Img}(x) \le T \\ \max(\operatorname{Img}_{5 \times 5}(x)) &, \max(\operatorname{Img}_{5 \times 5}(x)) - \operatorname{Img}(x) > T \end{cases}$$
 (1)

three times, where Img is the original image, x denotes a pixel in Img, Img' is the post-processed image, and $\max(\operatorname{Img}_{5\times 5}(x))$ is the maximal intensity within the 5×5 window in the neighborhood of x. In Equation 1, the pre-processing results are not sensitive to the threshold T, which is set to 5000 empirically for 16-bit images. The pre-processed line-center image is shown in the middle of Figure 1.

Post-flare loops of all the developing phases are recognized in the H α red-wing images. In the recognition procedure-multiple frames of H α red-wing images as well as the line-center images are used.

3. Methods

In the H α red-wing image, post-flare loops are dark, thin threads (Bruzek, 1964), which can also be seen in the right image of Figure 1. Therefore, some components of the loops could be roughly recognized by an edge-detection procedure. Then, a line-detection procedure is carried out to connect parts of the components belonging to a single loop. Since post-flare loops often occur as an arcade of loops whose feet form two parallel ribbons of $H\alpha$ emission in the chromosphere (Forbes, Malherbe, and Priest, 1989), it could be concluded that these loops tend to deflect to the flaring region when growing from the detected straight lines. To take advantage of this feature and make the recognition process easier, the flaring region is extracted from the Hα line-center image, as shown in the middle image of Figure 1. Based on the relationship between the detected straight lines and the flaring region, the blending orientation is determined. Finally, by combining pixels of similar intensity in a curve-growing process, each complete single loop is derived, followed by screening out false detections to accomplish the post-flare-loop detection procedure finally. As a consequence, the schematic of the proposed post-flare-loop detection method is shown in Figure 2, which mainly consists of five stages: edge detection, line detection, determination of blending orientation, curve growing, and eliminating wrong detections. Figure 3 illustrates the detection phases, and each step in Figure 2 is discussed in detail in Sections 3.1-3.5. The code of the proposed method is publicly available on github (github.com/PostFlareLoop/postflareloop).

3.1. Edge Detection

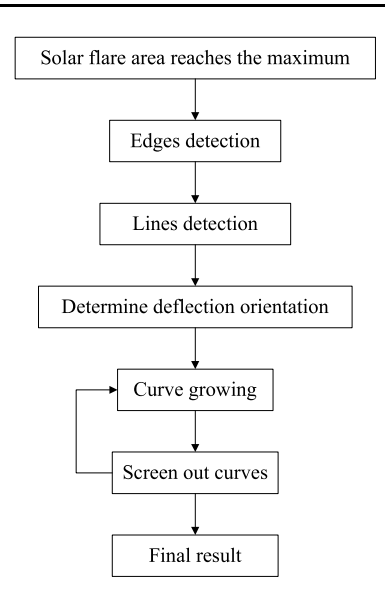
Generally, edges are the pixels with high gradients. In the process of detecting edges, the gradients of each pixel in four directions g_{hor} , g_{ver} , g_{diag1} , g_{diag2} are calculated, which denote the horizontal gradient, the vertical gradient, and the two diagonal gradients, respectively. Then the overall gradient g_{all} is computed in Equation 2 as

$$g_{\text{all}}(x, y) = \sqrt{g_{\text{ver}}^2(x, y) + g_{\text{hor}}^2(x, y) + g_{\text{diag1}}^2(x, y) + g_{\text{diag2}}^2(x, y)}.$$
 (2)

Pixels with g_{all} larger than 800 for 16-bit images are recognized as edges empirically. For the different temperatures, the intensity of the post-flare (4.5 × 10³ K) and the sunspot (10⁴ K) are empirically different (Solanki, 2003; Heinzel and Karlický, 1987). Therefore, by removing edges with high grayscale or near sunspot umbra, the edge-detection result is shown in Figure 3c.



Figure 2 Schematic of the proposed post-flare-loop detection method.



3.2. Line Detection

By finding lines in a parameter space, the Hough transform (Duda and Hart, 1972) is widely used to detect the presence of groups of colinear or almost colinear pixels. However, if straight lines are detected directly from the edges by the Hough transform, many false straight lines are induced by the interference between different components, as shown in Figure 4a. Connected components can be defined as a set of pixels that are adjacent to each other in the binary image. Consequently, in the line-detection procedure of the proposed method, all the connected components of the detected edges are extracted at first by the method proposed by Samet and Tamminen (1988), and then straight lines are detected within each component. Next, by removing components with small area or low eccentricity, stubby fragments are removed and the accuracy of line detection is improved substantially in Figure 4b. Since post-flare loops are aligned approximately parallel, those lines with different inclination angles, i.e. out of the range of 60 degrees, from the majority in Figure 4b are eliminated, and the rest are the green lines in Figure 4c. To further improve the true positive rate of line detection, the detected straight lines from the previous frame are added. The line-detection result is shown in Figure 3d and Figure 4c.

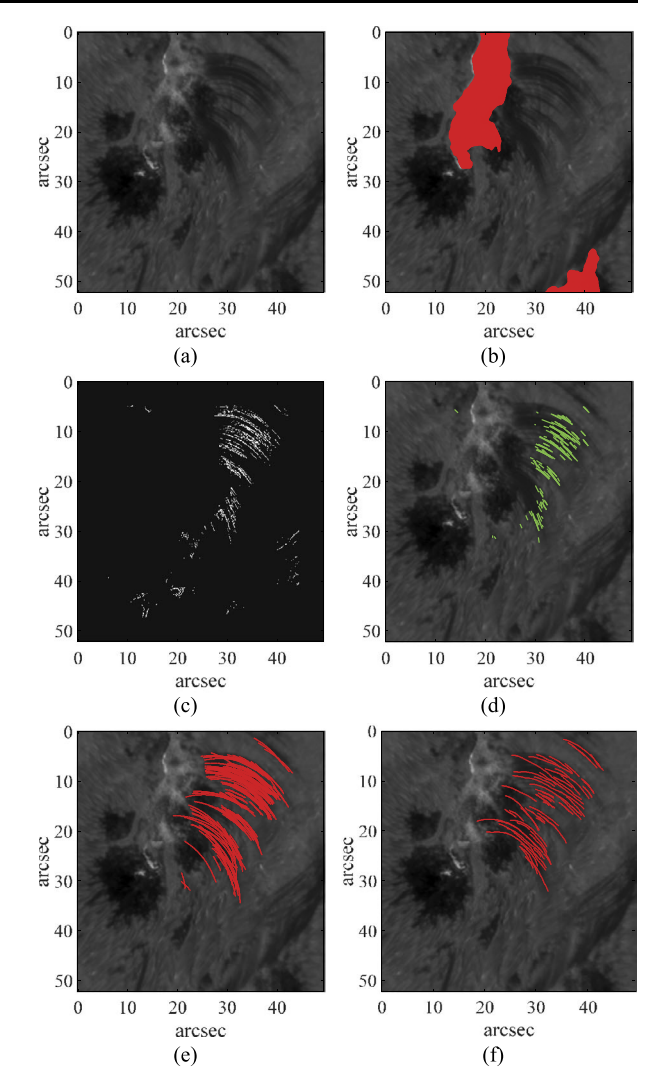
3.3. Blending Orientation Determination

The detected straight lines are just the stems of post-flare loops; the complete loops need to be grown from these straight lines in the curve-growing process. Similar to the regiongrowing method (Adams and Bischof, 1994), the so-called curve-growing method merges pixels with homogeneous properties to preassigned lines in two directions. As stated at the beginning of this section, post-flare loops have an arched shape with their feet forming the flaring region, so the blending orientation during the curve growing could be determined in advance to make the curve-growing results more reliable. The first step is to segment the flaring region from the Hα line-center image shown in the left image of Figure 1, and it could be achieved by the gray and area-threshold method (Yang et al., 2018). Owing to



62 Page 6 of 14 M. Yang et al.

Figure 3 Demonstration of the subsequent phases of the proposed post-flare-loop detection method. (a) The original image, the same as the right image in Figure 1; (b) the *red region* denotes the solar flare segmented from the $H\alpha$ line core image; (c) detected edges; (d) detected lines; (e) preliminary curve-growing result; (f) the post-flare-loop detection result.



the same recording time and field-of-view, the segmented flaring area in the $H\alpha$ line-center image could be labeled directly on the $H\alpha$ red-wing image, which is the red area in Figure 3b. As illustrated in Figure 5, the blending orientation, denoted by the yellow arrow, could be determined by the relationship between the inclination angles of the two yellow-dashed lines. One of the two yellow-dashed lines is the extension of the green line, the other refers to the plot between the green line-center and the nearest flare center, i.e. the blue circle. The direction of the yellow arrow means that the curve deflects anticlockwise when it grows upwards. The overall blending orientation is chosen to be the majority of all curves.

3.4. Curve Growing

The curve-growing process follows the determination of the overall blending orientation. In the case of merging bright pixels, each straight line is extended upwards and downwards



Figure 4 Phases of the line-detection procedure.
(a) detected lines from edges;
(b) detected lines within individual connected edges;
(c) the green lines are the results after removing lines with incorrect angles of inclination, and the red lines are the detected lines of the previous frame. The green and red lines form the detected lines of the current frame

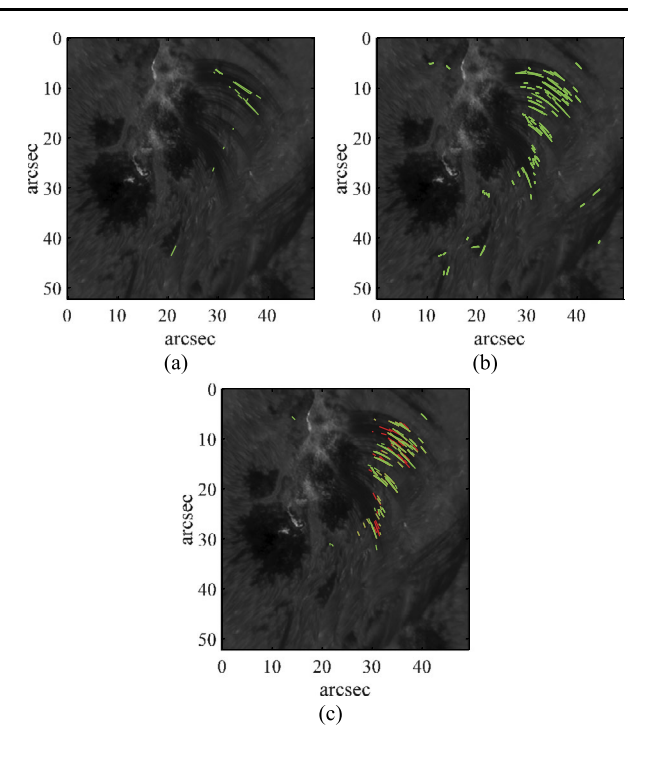
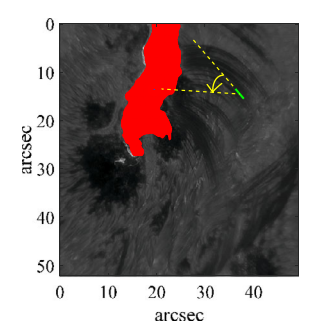


Figure 5 Schematic of determining curve-growing blending orientation. The *green line* denotes a detected line in the previous stage; the *red area* is the flare region nearest to the *green line*; the *blue circle* is the flare center; the *yellow-dashed lines* are the extension of the *green line-center* and the flare center; the *yellow arrow* represents the blending orientation.



until the intensity of the grown point exceeds 1.2 times that of the starting point. Combining the pixel with the intensity closest to the seed pixel in each iteration may be simple and effective in some cases, but it is not always the optimal option, especially when many loops overlap with each other. To improve the reliability of the proposed method, the grown curve with great length and high intensity homogeneity is chosen from n candidates (n is set to 3 in Figure 6, i.e. the grown curve has the largest qua(i) in Equation 5) when the curve-growing process stops. During the process, the inclination angle of each grown point could be calculated as

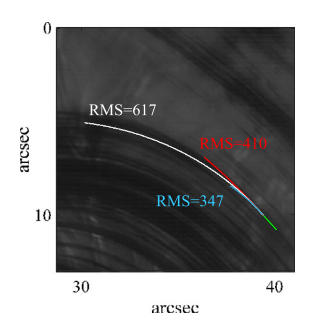
$$\theta_t = \theta_0 - d \times len_t \times r,\tag{3}$$

where θ_t is the inclination angle at the current point, and θ_0 is the inclination angle of the straight line. θ_t and θ_0 are in the range from -90° to 90° . -90° refers to horizontally left-



62 Page 8 of 14 M. Yang et al.

Figure 6 Schematic of determining the blending angle of curve-growing.



ward, 0° refers to vertically upward, and 90° refers to horizontally rightward. d denotes to the blending orientation. d=1 means that the curve deflects anticlockwise when growing upwards and clockwise when growing downwards, while d=-1 refers to the opposite. len_t is the current length of the extension from the straight line, which increases by 1 with each pixel added. r is the blending fraction calculated as

$$r = r_0 \times i, \ i = 1, 2, ..., n,$$
 (4)

where r_0 is an empirical parameter set to 0.2 in the application. The quality of each candidate could be evaluated as

$$qua(i) = \frac{len(i)}{\min(len)} \times \frac{\max(RMS)}{RMS(i)}, i = 1, 2, ..., n,$$
(5)

where *len* denotes the length of the grown curve, and *RMS* denotes the root-mean-square intensity of the curve pixels. *n* is the number of grown curves. The curve corresponding to the largest *qua* is the final result of the curve growing. As illustrated in Figure 6, the green line is the detected straight line. The red, white, and cyan curves are three candidates for the grown curve. Although the *RMS* of the red and cyan curves are less than the white curve, the *len* of the white curve is greater than the others. Thus the white curve gains the highest *qua* and is chosen to be the grown curve. Up to this point, the preliminary curve-growing result is derived, as shown in Figure 3e.

3.5. Screening Out False Detection

The stage of screening out curves is to eliminate these false detections. As shown in Figure 3e, some isolated curves do not belong to the post-flare loops. At the same time, there are many intersections in the preliminary curve-growing result. The post-flare loops arrange closely, so a grown curve would easily intersect other curves if the blending angle deviates a little bit. Therefore, the stage consists of two steps: In the first step, the distances between the centers of every two curves are calculated, and the isolated curves, which are far away from all other curves, are eliminated. The second step is used to reduce the intersections between the curves and consequently the false-positive rate of the post-flare-loop detection. The schematic of removing intersected curves is shown in Figure 7, where i has the same meaning as in Equation 4 and Equation 5. Firstly, we find the curve with the most intersections and carry out the curve-growing process from the corresponding straight line iteratively. Compared with the curve-growing process in the previous stage, the curve stops growing when it intersects other curves immediately in this stage. The above-mentioned steps are repeated in this stage until the iteration j exceeds 50 or the maximal intersections



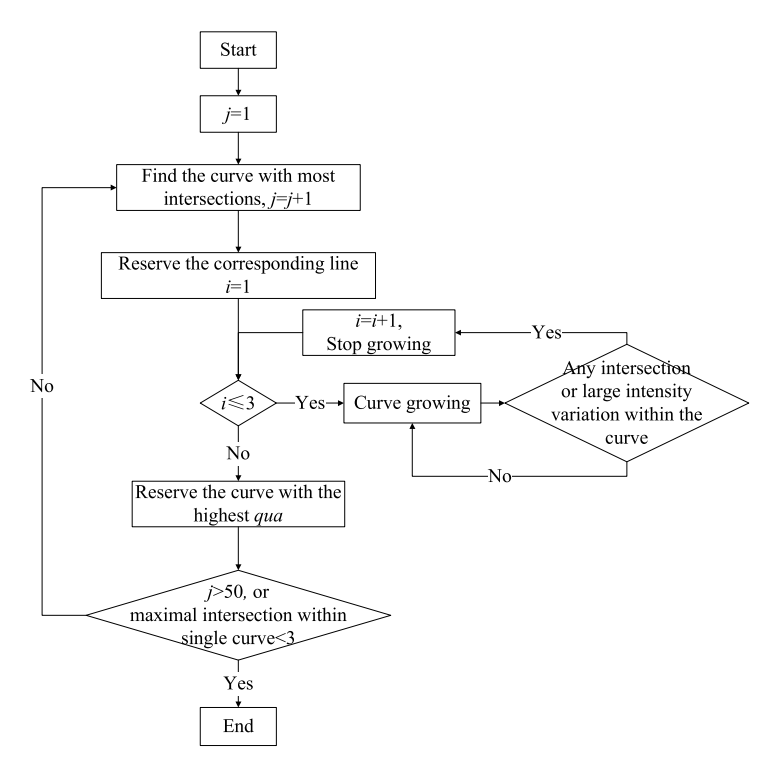


Figure 7 Schematic of reducing intersections between curves.

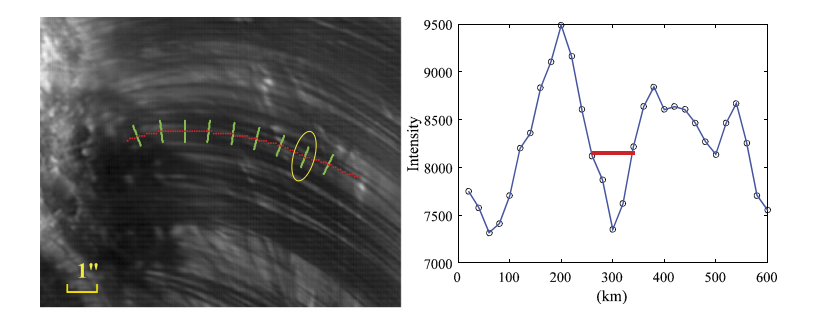


Figure 8 The determination of the loop widths. In the left image, the red curve is a detected loop, and the green lines are some perpendicular lines of the loop to label cross-sectional slits. In the right image, the intensity variations along the green line, which is enclosed by a yellow circle in the left image, are shown, and the red line refers to the FWHM.

within a single curve are less than 3. It can be seen that intersections in Figure 3f, i.e. the final result of post-flare-loop detection, is less than in Figure 3e.

Based on the recognition results of the post-flare loops, the cross-sectional full width at half maximum (FWHM) of these loops are measured. As shown in the left image of Figure 8, the perpendicular lines are labeled automatically according to the inclination angles at the uniformly sampled points of the loop. The right image of Figure 8 illustrates the intensity variations along the green line and the determination of the FWHM.



62 Page 10 of 14 M. Yang et al.

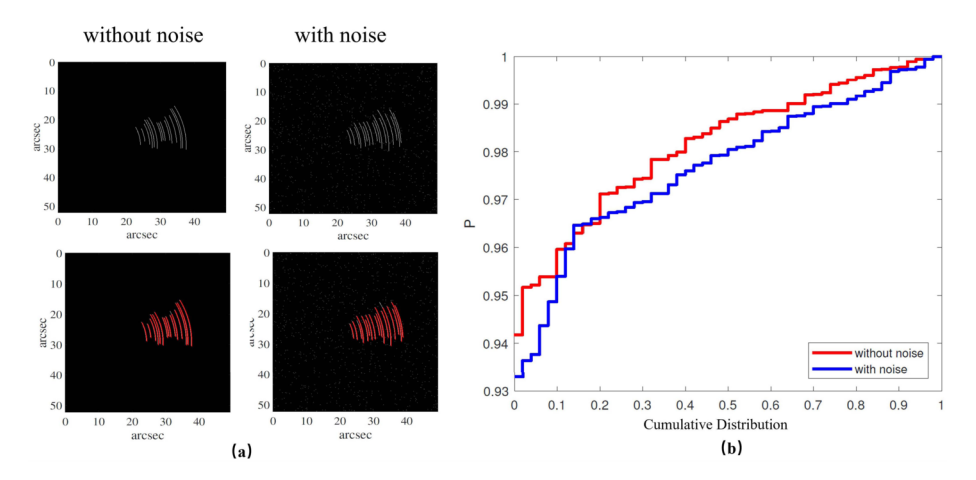


Figure 9 (a) The representative examples of dummy data set. (b) The cumulative distribution of P.

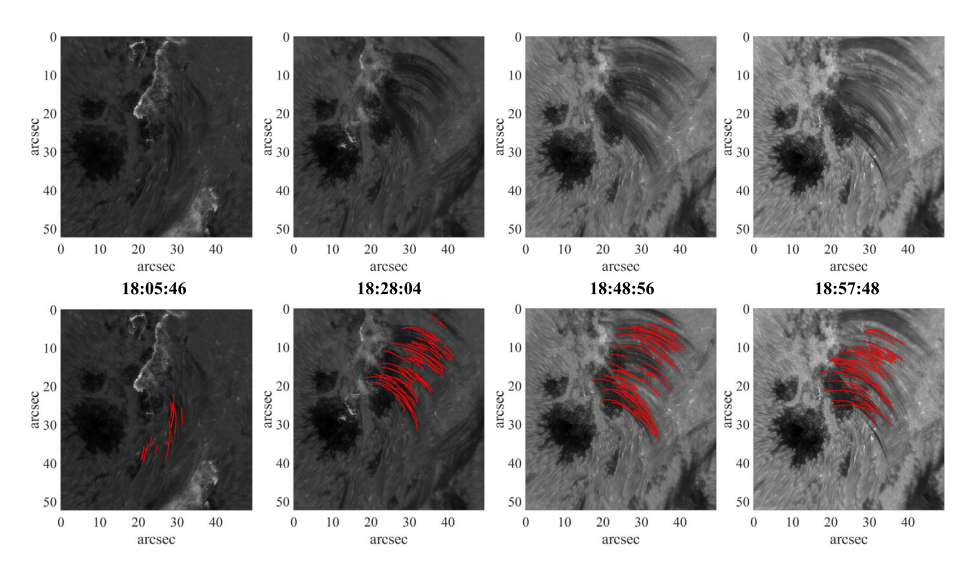


Figure 10 The post-flare-loop recognition results of the M6.5 solar flare on 22 June 2015, using GST high-resolution $H\alpha+1.0$ Å images. The speckle-reconstructed images are at the *top row*, the corresponding times are in the *middle*, and the *red curves* in the images at the *bottom row* are the detected post-flare loops.

4. Experimental Results

Figure 9 gives the results of the proposed method running on a dummy data set. The dummy data contains 100 randomly generated data, of which 50 are without noise and 50 with noise. In Figure 9a, two representative images with and without noise and their recognition results are shown. In order to quantitatively evaluate the performance of the proposed method more intuitively, this article uses the performance-measure method proposed by Grigorescu, Petkov, and Westenberg (2003). Let E_{GT} and E_{D} be the ground truth of the loop coordinates of the dummy data and the coordinates of the loops given by the proposed method, respectively. The set of correctly detected loops is $E = E_{D} \cap (E_{GT} \oplus T)(\bigoplus)$ is the image dilation



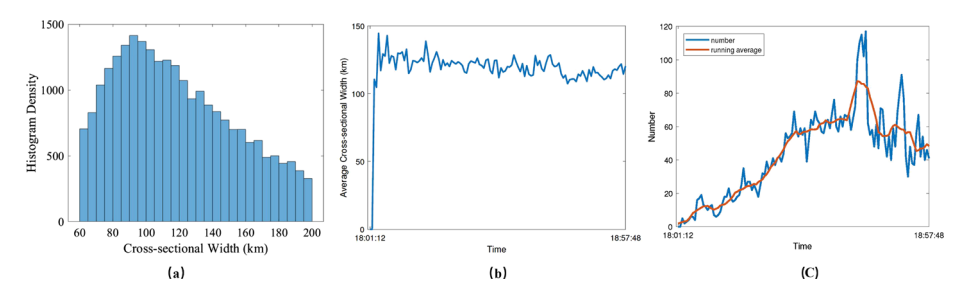


Figure 11 (a) Histogram of the cross-sectional FWHM of post-flare loops based on a sample of 24,765 slits within 120 images. (b) The change in the average cross-sectional width of the post-flare loops over time. (c) The change in the number of post-flare loops over time.

operation and T is a 5×5 structure element). False positives are given by $E_{FP} = E_D - E$ and false negatives are given by $E_{FN} = E_{GT} - (E_{GT} \cap (E_D \bigoplus T))$. The performance measure P can be defined as

$$P = \frac{card(E)}{card(E) + card(E_{FP}) + card(E_{FN})},$$
(6)

where card(X) denotes the number of elements in X. The averages P are 0.982 ± 0.015 and 0.977 ± 0.017 for the data sets without and with noise, respectively. Figure 9b shows the cumulative distribution of P obtained by the proposed method executed on the dummy data set. We can observe from Figure 9 that our method can achieve good results for both data without noise and data with noise.

Figure 10 gives the post-flare-loop detection result of the M6.5 solar flare on 22 June 2015, using the GST high-resolution $H\alpha+1.0$ Å images. The red curves in the images in the bottom row of Figure 10 are the recognized post-flare loops. Considering that each loop is a collection of overlapped and unresolved strands that are heated at different times, it is concluded that the proposed method can derive acceptable results at all the developing phases of post-flare loops.

As shown in Figure 11a, 24,765 FWHM data were computed from the 120 frames of $\rm H\alpha$ red-wing images captured from 18:01:40 to 18:57:48. Only the widths in the range of 60-200 km are reserved. The FWHM data are distributed with an average of 118 ± 35 km, roughly in accordance with the data, 124 ± 19 km, computed from 107 loops by Jing et al. (2016). Compared with the manual method for computing loop widths, the proposed method could collect large datasets and derive consistent width results. In addition, we show the changes in the average cross-sectional width and the number of post-flare loops through time in Figure 11b and c. The running average is also plotted in Figure 11c, using a moving window with a width of 10 frames. As shown in Figure 11c, our algorithm finds 5,227 post-flare loops from 120 frames, with an average of about 44 loops per frame. A large number of post-flare loops are found in the second half of the data (i.e. in the last 60 frames), a total of 3,718, and the average number of loops per frame is about 62 in the last 60 frames.

5. Conclusion

In this article, an automated post-flare loop recognition method applied to high-resolution $H\alpha$ red-wing images has been developed, and we published the code on github (github.



62 Page 12 of 14 M. Yang et al.

com/PostFlareLoop/postflareloop). The proposed method mainly consists of five stages: edge detection, line detection, determining blending orientation, curve growing, and screening out curves. When determining the blending orientation, the $H\alpha$ line-center image with the same recording time is used to segment the flaring region. Based on the loop-recognition results, the loop widths are computed automatically and a result consistent with the manual method is derived.

Although the fine structures of the post-flare loops could not be resolved with the instrumentation available, the proposed method shows the potential to derive more accurate recognition results with future telescopes, and our measurements bridge the gap between theoretical simulation and observations. In the future, data-mining approaches could be used to objectively determine the best values for some empirical parameters based on the analysis of more data.

The post-flare loop is a typical dynamic process of a solar flare. With higher resolving power, more strands inside the loop are resolved. Therefore, the automatic post-flare-loop recognition method proposed makes fast and reliable loop recognition available. The statistical results, such as the number, width, and duration of the post-flare loop, based on this recognition method can be obtained conveniently. It would be a useful tool for studies on statistical and physical relationships among the post-flare loops.

Acknowledgment We gratefully acknowledge the use of data from the *Goode Solar Telescope* (GST) of the Big Bear Solar Observatory (BBSO). BBSO operation is supported by NJIT and US NSF AGS-1821294 grant. GST operation is partly supported by the Korea Astronomy and Space Science Institute and the Seoul National University.

Author Contribution Meng Yang and Xiaoying Gong contributed equally to this work. They completed the writing, experimentation, and revision of the article. Yangyi Liu and Yu Tian collected data and made suggestions on the method of the article. Changhui Rao supervised this work.

Funding This work was supported by Natural National Science Foundation of China (NO.11727805 and NO.11703029) and the Laboratory Innovation Foundation of the Chinese Academy of Sciences (Grant NO. YJ16K006).

Code Availability The code of the proposed method has been published on github: github.com/Post-FlareLoop/postflareloop.

Declarations

Disclosure of Potential Conflicts of Interest The authors declare that they have no conflicts of interest.

References

Adams, R., Bischof, L.: 1994, Seeded region growing. IEEE Trans. Pattern Anal. Mach. Intell. 16, 641. DOI.
Antolin, P., Rouppe van der Voort, L.: 2012, Observing the fine structure of loops through high resolution spectroscopic observations of coronal rain with the CRISP instrument at the Swedish Solar Telescope. Astrophys. J. 745, 152. DOI. ADS.

Aschwanden, M.J.: 2010, A code for automated tracing of coronal loops approaching visual perception. Solar Phys. 262, 399. DOI. ADS.

Bruzek, A.: 1964, On the association between loop prominences and flares. Astrophys. J. 140, 746. DOI. ADS.

Cao, W., Gorceix, N., Coulter, R., Ahn, K., Rimmele, T.R., Goode, P.R.: 2010, Scientific instrumentation for the 1.6 m New Solar Telescope in Big Bear. Astron. Nachr. 331, 636. DOI. ADS.

Cargill, P.J.: 1994, Some implications of the nanoflare concept. Astrophys. J. 422, 381. DOI. ADS.



- Cargill, P.J., Klimchuk, J.A.: 2004, Nanoflare heating of the corona revisited. Astrophys. J. 605, 911. DOI.
- Cheng, X., Ding, M.D., Guo, Y., Zhang, J., Jing, J., Wiegelmann, T.: 2010, Re-flaring of a post-flare loop system driven by flux rope emergence and twisting. Astrophys. J. Lett. 716, L68. DOI. ADS.
- Denker, C., Johannesson, A., Marquette, W., Goode, P.R., Wang, H., Zirin, H.: 1999, Synoptic Hα full-disk observations of the Sun from Big Bear Solar Observatory – I. Instrumentation, image processing, data products, and first results. Solar Phys. 184, 87. DOI. ADS.
- Duda, R.O., Hart, P.E.: 1972, Use of the Hough transformation to detect lines and curves in pictures. Commun. ACM 15, 11. DOI.
- Durak, N., Nasraoui, O., Schmelz, J.: 2009, Coronal loop detection from solar images. Pattern Recognit. 42, 2481. DOI.
- Forbes, T.G., Malherbe, J.M., Priest, E.R.: 1989, The formation of flare loops by magnetic reconnection and chromospheric ablation. Solar Phys. 120, 285. DOI. ADS.
- Grigorescu, C., Petkov, N., Westenberg, M.A.: 2003, Contour detection based on nonclassical receptive field inhibition. IEEE Trans. Image Process. 12, 729.
- Heinzel, P., Karlický, M.: 1987, Hα diagnostics of (post)-flare loops based on narrow-band filtergram observations. Solar Phys. 110, 343. DOI. ADS.
- Inhester, B., Feng, L., Wiegelmann, T.: 2008, Segmentation of loops from coronal EUV images. Solar Phys. 248, 379, DOI, ADS.
- Jing, J., Xu, Y., Cao, W., Liu, C., Gary, D., Wang, H.: 2016, Unprecedented fine structure of a solar flare revealed by the 1.6 m New Solar Telescope. Sci. Rep. 6, 24319. DOI. ADS.
- Kamio, S., Kurokawa, H., Ishii, T.T.: 2003, Precise determination of cooling times of post-flare loops from the detailed comparison between Hα and soft X-ray images. Solar Phys. 215, 127. DOI. ADS.
- Klimchuk, J.A.: 2006, On solving the coronal heating problem. Solar Phys. 234, 41. DOI. ADS.
- Lin, J., Zhang, Z., Wang, Z., Smartt, R.N.: 1992, The morphological characteristics and cooling mechanisms of the post-flare loop system of April 28, 1980. Astron. Astrophys. 253, 557. ADS.
- McAteer, R.T.J., Kestener, P., Arneodo, A., Khalil, A.: 2010, Segmentation of loops from coronal EUV images. Solar Phys. 262, 387. DOI. ADS.
- Podgorny, A.I., Podgorny, I.M.: 2002, Numerical MHD simulations of post-flare loop formation on the Sun allowing for thermal-conductivity anisotropy. Astron. Rep. 46, 67. DOI. ADS.
- Reeves, K.K., Warren, H.P.: 2002, Modeling the cooling of postflare loops. Astrophys. J. 578, 590. DOI. ADS.
- Rimmele, T.R., Warner, M., Keil, S.L., Goode, P.R., Knölker, M., Kuhn, J.R., Rosner, R.R., McMullin, J.P., Casini, R., Lin, H., Wöger, F., von der Lühe, O., Tritschler, A., Davey, A., de Wijn, A., Elmore, D.F., Fehlmann, A., Harrington, D.M., Jaeggli, S.A., Rast, M.P., Schad, T.A., Schmidt, W., Mathioudakis, M., Mickey, D.L., Anan, T., Beck, C., Marshall, H.K., Jeffers, P.F., Oschmann, J.M., Beard, A., Berst, D.C., Cowan, B.A., Craig, S.C., Cross, E., Cummings, B.K., Donnelly, C., de Vanssay, J.-B., Eigenbrot, A.D., Ferayorni, A., Foster, C., Galapon, C.A., Gedrites, C., Gonzales, K., Goodrich, B.D., Gregory, B.S., Guzman, S.S., Guzzo, S., Hegwer, S., Hubbard, R.P., Hubbard, J.R., Johansson, E.M., Johnson, L.C., Liang, C., Liang, M., McQuillen, I., Mayer, C., Newman, K., Onodera, B., Phelps, L., Puentes, M.M., Richards, C., Rimmele, L.M., Sekulic, P., Shimko, S.R., Simison, B.E., Smith, B., Starman, E., Sueoka, S.R., Summers, R.T., Szabo, A., Szabo, L., Wampler, S.B., Williams, T.R., White, C.: 2020, The Daniel K. Inouye Solar Telescope – observatory overview. Solar Phys. 295, 172. DOI. ADS.
- Sakamoto, Y., Tsuneta, S., Vekstein, G.: 2008, Observational appearance of nanoflares with SXT and TRACE. Astrophys. J. 689, 1421. DOI. ADS.
- Samet, H., Tamminen, M.: 1988, Efficient component labeling of images of arbitrary dimension represented by linear bintrees. IEEE Trans. Pattern Anal. Mach. Intell. 10, 579. DOI.
- Scharmer, G.B., Narayan, G., Hillberg, T., de la Cruz Rodriguez, J., Löfdahl, M.G., Kiselman, D., Sütterlin, P., van Noort, M., Lagg, A.: 2008, CRISP spectropolarimetric imaging of penumbral fine structure. Astrophys. J. Lett. 689, L69. DOI. ADS.
- Scullion, E., Rouppe van der Voort, L., Wedemeyer, S., Antolin, P.: 2014, Unresolved fine-scale structure in solar coronal loop-tops. Astrophys. J. 797, 36. DOI. ADS.
- Sellah, S., Nasraoui, O.: 2008, An incremental Hough transform for detecting ellipse in image data streams. In: 20th IEEE International Conference on Tools with Artificial Intelligence 2, 45. DOI.
- Solanki, S.K.: 2003, Sunspots: an overview. Astron. Astrophys. Rev. 11, 153. DOI. ADS.
- Srivastava, A.K., Zaqarashvili, T.V., Uddin, W., Dwivedi, B.N., Kumar, P.: 2008, Observation of multiple sausage oscillations in cool post-flare loop. Mon. Not. Roy. Astron. Soc. 388, 1899. DOI. ADS.
- Vekstein, G.: 2009, Probing nanoflares with observed fluctuations of the coronal EUV emission. Astron. Astrophys. 499, L5. DOI. ADS.
- White, R.S., Verwichte, E., Foullon, C.: 2012, First observation of a transverse vertical oscillation during the formation of a hot post-flare loop. Astron. Astrophys. 545, A129. DOI. ADS.



62 Page 14 of 14 M. Yang et al.

Yang, M., Tian, Y., Liu, Y., Rao, C.: 2018, Automated solar flare detection and feature extraction in high-resolution and full-disk Hα images. *Solar Phys.* 293, 81. DOI. ADS.

Publisher's Note Springer Nature remains neutral with regard to jurisdictional claims in published maps and institutional affiliations.

